Aptamer functionalized ZnO thin-film transistor based multiplexed detection of Lead and E. coli in water

Sanath Kumar Honnali
Indian Institute of Science
Vikram Srinivasa Raghavan (vikrams@iisc.ac.in)
Indian Institute of Science
Roopa Ashwath
Indian Institute of Science
Ganapathy Saravanavel
Indian Institute of Science
K R Gunasekhar
Indian Institute of Science
Sanjiv Sambandan
Indian Institute of Science
Sai Siva Gorthi
Indian Institute of Science
Benjamin O'Driscoll
Plymouth University
David Jenkins
Plymouth University

Research Article

Keywords: Aptamer, E. coli, Pb2+, TFT array, ZnO

Posted Date: May 3rd, 2022

DOI: https://doi.org/10.21203/rs.3.rs-1593963/v1

RESEARCH

Aptamer functionalized ZnO thin-film transistor based multiplexed detection of Lead and E. coli in water

Sanath Kumar Honnali[1], Vikram Srinivasa Raghavan[1*], Roopa Ashwath[1], Ganapathy Saravanavel[1], K R Gunasekhar[1], Sanjiv Sambandan[1], Sai Siva Gorthi[1], Benjamin O'Driscoll[2] and David Jenkins[2]

Abstract

Background: Contamination of lead (Pb^{2+}) disturbs biological functions and causes neurotoxicity even at low levels. Pathogens such as *Escherichia coli*, *P. aeruginosa* and *S. aureus* found in packaged drinking water causes infections. Therefore, we demonstrate the multiplexed detection of Pb^{2+} and *E. coli* in water using ZnO thin-film transistor (TFT) arrays.

Results: Low voltage ZnO TFTs fabricated by physical vapour deposition were functionalized with APTES-glutaraldehyde molecules. TFTs with such functionalized ZnO surfaces showed good sensitivity and high specificity to the targets. The TFTs showed a detection limit of 27 nM and 10^5 cfu/ml for Pb^{2+} and *E. coli*, respectively with the TFT flat-band voltage (V_{fb}), and hence the TFT transconductance, being dependent on the target concentration. The direct integration of the sensing with the TFT and associated integrated circuits promises high density sensor arrays.

Conclusion: The present work highlights the importance of aptamers in the multiplexed detection of different targets using low cost ZnO TFT array.

Keywords: Aptamer; *E. coli*; Pb^{2+}; TFT array; ZnO

Introduction

Thin-film transistors (TFTs) are the building blocks of technologies such as flexible electronics, large area electronics and wearable electronics. The emergence of new manufacturing technologies such as inkjet printed electronics, along with the possibility of using the TFT as a field effect sensor promises low cost, low power, large area, smart surfaces where the sensing operation is directly integrated with the signal processing.

Recently, TFTs have been investigated for applications related to environmental monitoring and biosensing, e.g. in the detection of Hg^{2+} [1], Pb^{2+} [2], Cu^{2+} [3], Cd^{2+} [4] and As [5], *E. coli* [6, 7, 8], *E. faecalis* [8] and *S. aureus* [9].

In this work, we specifically consider the problem of detection of Pb^{2+} and *E.coli* contamination in water. Both, Pb^{2+} and *E.coli* are known to be serious contaminants in water. Even low levels of Pb^{2+} disturbs biological functions [10] and causes neurotoxicity [11, 12, 13], while pathogens such as *E.coli*, *P. aeruginosa* and *S. aureus* found even in packaged drinking water [14] causes infections[15].

To address this problem, several low-cost portable devices have been developed and shown to have good success [16, 17, 18, 19, 20, 21, 22]. More recently, DNA based biosensors have been shown to be very effective in detecting various contaminants in water [23, 24, 25]. DNA based sensors have been integrated with optical, electrical and electrochemical systems and techniques for the detection of heavy metals and pathogens [26, 27, 28]. While each sensing technique has its own advantages and limitations [29], the limitations of electrical sensing techniques were overcome by the use of aptasensors which permitted high specificity [28, 30, 31] and the possibility of integration with transistors [32, 33, 34, 35].

In this work, we develop aptamer functionalized zinc oxide (ZnO) TFTs for the detection of Pb^{2+} and *E.coli* in water. ZnO TFTs are a class of metal oxide TFTs and are intrinsically n-type and show reasonably high mobility (about 10 cm^2/Vs) [36]. They are environmentally stable and non-toxic and have been used for

*Correspondence: vikrams@iisc.ac.in
[1]Department of Instrumentation and Applied Physics, Indian Institute of Science, Bengaluru, 560012, India
Full list of author information is available at the end of the article

applications such as the detection of sensitive cardiac biomarkers like troponin I [37] and troponin-T [38]. Specific to this work, ZnO based thin films were functionalized using (3- Aminopropyl) triethoxysilane (APTES). This process enables the immobilization of different antibodies and aptamers with various functional groups [39]. The aptamer functionalized ZnO TFTs were then shown to experience a change in the flat-band voltage when exposed to Pb^{2+} and *E. coli* species. This change in flat-band voltage effectively translates to a change in the current-voltage characteristics of the TFT which is measured to quantify the change. This work promises the direct integration of water contaminant sensors with TFT based integrated circuits thereby enabling direct signal processing.

Experimental section

Materials

Corning glass of 75 mm × 25 mm × 1 mm dimensions was used for device fabrication. 99.9% pure zinc (Zn) sputter target, Aluminium oxide pellets (3mm) and 1 mm diameter pure aluminium wire used for fabrication were purchased from Sigma-Aldrich. Lead(II) nitrate (99%) was purchased from SRL Chemical, India. Ultra pure oxygen and Argon gases were purchased from Noble gases Pvt. Ltd, Bengaluru, India. Tungsten helical filaments for resistive evaporation were purchased from VR Technologies Pvt. Ltd, Bengaluru, India. Isopropyl alcohol (99%), (3-Aminopropyl) triethoxysilane 99% was purchased from Sigma-Aldrich, Glutaraldehyde solution 25% was purchased from SD Fine-Chem Limited, Maharashtra, India. Aptamer sequences were purchased from GCC Biotech Pvt. Ltd., West Bengal, India.

Methods

Bacterial strain, media and culture conditions

The non-pathogenic strains of *Escherichia coli* and *Klebsiella pneumoniae* (*KP*) were selected for this study. Cultures were grown on Luria Bertani (LB) medium. Pure colonies of cultures were obtained by streak plate technique using LB agar medium. The cultures were incubated at 37°C for 12-14 hours. Individual colonies were selected and transferred to LB broth. The broth cultures were incubated in a shaking incubator at 37°C for 12-14 hours at 100-120 rpm. To determine the cfu/ml, the broth cultures were diluted and plated using the spread plate technique. The cfu/ml for *E.coli* broth was found to be 2×10^{11} cfu/ml and that of *Klebsiella pneumonia*e was found to be 5×10^{11} cfu/ml. For the purpose of this study, a known volume of stock broth culture was diluted 1000 times in LB broth for easy detection and analysis.

TFT fabrication

Fig. 1(a:top) depicts the cross section view of the bottom inverted gate structure of the thin-film transistor (TFT). Aluminium was used as the gate and drain source electrodes. Aluminium oxide (Al_2O_3) and zinc oxide were used as the dielectric and semiconducting materials, respectively. The stacked layers have a thickness of 150 nm, 300 nm, 100 nm and 150 nm of gate, dielectric, semiconductor, drain source layers from bottom to top, respectively. The electrodes were deposited by resistive evaporation, ZnO by reactive DC magnetron sputtering and Al_2O_3 by e-beam evaporation methods [Fig S1]. ZnO with oxygen content of 80.45% showed excellent semiconducting properties with a band gap of 3.25 eV [see Additional file 1]. Fig. 1(a:bottom) depicts the 3D view of the TFT structure. Fig. 1(b:top) shows the microscopic view of the semiconductor channel length (L) of ∼50 μm. Fig. 1(b:bottom) shows the 3D view of an array of three TFTs having a common gate electrode. The same structure was replicated thirteen times horizontally and twice vertically to fit the working area on the corning glass. Fig. 1(c) shows the final image of the TFT array consisting of 78 TFTs with consumable cost of ∼ $0.04 per device.

Surface functionalisation and characterisation of the sensor

The ZnO surface was purged with nitrogen. A 10 μL volume of 1% (V/V) APTES solution in 95% ethanol was prepared and 2 μL was added on the ZnO surface. This was further heated for 15 min at 75°C in an inert chamber. The APTES modified ZnO surface was then repeatedly washed with ethanol to remove any unbound silane. Then 2 μL of glutaraldehyde was added on top and heated at 55°C for 10 minutes. Fig. 1(d) represents the close-up view of the ZnO surface functionalized with APTES and glutaraldehyde (GLU) molecules. For characterization of the devices, IR analysis was performed for TFT sensors using the Attenuated Total Reflectance (ATR) mode in FTIR (PerkinElmer, USA) with the operational range 7800-650 cm^{-1}. AFM studies were also conducted using Park NX20 AFM (Park Systems, South Korea) and the plots were generated using Park Systems XEI software 4.3. Later, I-V characteristics for TFTs were performed using Keithley 4200-SCS system. Eventually, 1 μL of aptamer was added and incubated for 20 min at room temperature. Then prior said measurements were carried out before adding the targets (1 μL) and incubated at same conditions. Different incubation periods were carried out up to 40 min, out of which a minimum 20 min was observed to be optimum incubation time for I-V sweep. Fig. 1(e & f) depicts the attachment of aptamer appropriate to bind the lead (Pb^{2+}) ions and *E. coli*, respectively. The microscopic image of *E. coli* was captured during the live test when immobilized on the aptaTFT surface.

Results and Discussion

TFT electrical characteristics

TFTs with minimum off current (I_{off}) enable detection of targets with low concentrations. In order to achieve a low off current, it is necessary to have a low free carrier concentration. The latter was achieved by increasing the oxygen partial pressure during the fabrication stage [40]. Fig. 2(a) shows the transfer characteristics of the bare TFT at $V_{ds} = 5$V. The gate voltage was swept from -8 to +8V keeping the drain voltage constant (varied from 0 to 5V in 1V steps). The inset in Fig. 2(a) represents the range of the flat-band voltage (V_{fb}) and current at this voltage (I_{fb}) for ten similar devices. The ten devices were chosen across the TFT array and the devices performance was fairly consistent across the array with I_{on}/I_{off} ratio of 10^2. The output characteristics of the TFT were also studied by varying the drain voltage from 0 to 5V at a constant gate voltage, which was varied from 0 to 6V in steps of 2V and is shown in Fig. 2(b).

Chemical analysis

FTIR-ATR method was used to analyze the samples. In Fig. 3(a), peaks at 2865 cm^{-1} and 2726 cm^{-1} are attributed to C-H (propyl groups) and aldehyde-CHO, which originates from glutaraldehyde [41]. In Fig. 3(b), the interaction of glutaraldehyde with APTES was observed. Peaks related to the NH_2 group are observed at 1566 cm^{-1}, C=O at 1713 cm^{-1} and 1099 cm^{-1} for Si-O-Si [42, 43, 44]. Fig. 3(c & d) shows NHPb aptamer interaction with glutaraldehyde. Peaks at 2362 cm^{-1} and 3388 cm^{-1} correspond to C-H alkyl spacer (smoothed form shown in Fig. 3(d) [inset]) and NH_2 groups present in the aptamer [45, 41]. These peaks confirm the interaction between glutaraldehyde and aptamers. The signals originating from these peaks confirm the aptamers bound to the ZnO sensor surface through APTES-GLU cross-linker. Due to the strong absorption of other functional groups, peaks attributed to DNA could not be observed in these spectra [46].

Surface analysis

AFM images of ZnO-TFTs with APTES-GLU and aptamer are presented in Fig. 4. Fig. 4(a) shows the 2D image of APTES-GLU with RMS roughness value Rq=19.941 and Ra=15.007 with the focus area of 3 μm by 3 μm. Fig. 4(c) shows the 2D image of APTES-GLU-DNA with RMS roughness value Rq=29.74 and Ra=22.042 with the focus area of 3 μm by 3 μm respectively. RMS has increased with a shift of ~9.7 nm in Rq indicating the addition of 100 nM of NHPb aptamers conjugation to the APTES-GLU linker. The aptamers were added to the TFTs and vacuum dried for 60 mins before recording AFM images. Fig. 4(b & d) shows 3D images of APTES-GLU and APTES-GLU-DNA, respectively (focus area 0.5 μm by 0.5 μm) indicating a change in the surface pattern after the addition of aptamer. Fig. 4(e & f) shows 3D images with a larger focus area of 2 μm by 2 μm, shows the transformation in the ZnO surface after functionalization (APTES-GLU) followed by DNA incubation.

Effect on electrical characteristics of the TFT

To understand the mechanism of the TFT based sensing, one needs to understand the underlying physics in the operation of the bare TFTs. A voltage bias applied to the gate electrode creates an electric field in the channel. This field attracts and accumulates free electric charges of opposite sign in a thin layer of semiconductor near the dielectric interface. The basic idea behind the present sensor to detect various targets, is to study the effect of the charges induced by the targets on the ZnO surface. These extra charges either positive or negative represent the charged targets after being captured on the channel's surface.

Therefore, modification of the semiconductor channel surface by the targets will directly influence the characteristic parameters of the TFT such as flat-band voltage and mobility (μ). Optimisation was carried out on the device dimension, material properties in accordance with the applications' need. However, surface modification was done by a chemical method of surface functionalization. This allows the user to alter the surface property by choosing the appropriate chemical functional groups. Since ZnO shows n-type behaviour [47], the more electro-positive end of the APTES when added, will attach to the ZnO surface [Fig. 1(d)] would result in a field that induces electrons near the semiconductor-insulator interface [48, 49]. Essentially, this can be viewed as a reduction in flat band voltage. For all concentrations of APTES-GLU, the flat band voltage remained confined around -3.725 V with a deviation of ±0.5 V. Therefore, this result signifies that there is a chemical change on the surface of the semiconductor layer which is confirmed by FTIR studies [Fig. 3]. After the addition of the aptamer, the V_{fb} increases and shifts towards the positive direction though remaining in the negative V_{gs} region. This means more number of electrons are attached to the other end of the APTES due to the aptamer. This reduces the potential at the APTES-ZnO interface which depletes the electrons at the semiconductor-dielectric interface and results in lowering the drain current (I_{ds}). Moreover, these results allow us to observe that the chemical processes do not damage the electrical response of the transfer characteristics of ZnO TFTs before and after the aptamer immobilization.

Pb^{2+} detection

The aptamers tend to form G-quadruplex after binding with the target. Fig S2 shows the possible secondary structure of these aptamers with table [inset] highlighting the sequences with number of guanine bases. Typically, nucleobases like guanine and thymine contribute to a high specificity towards binding with the target molecules. Among these, G-quadruplex is thermally stable, formed by guanine rich sequences. G-quadruplex also contributes high specificity towards target molecules [50]. G-quadruplex based-detection shows a promising trend for selective determination of heavy metal ions [51, 52, 53] and pathogens [54, 55]. Guanine rich oligonucleotides favor detection of Pb^{2+} by forming a G-quadruplex structure with high specificity. This structure exhibits good stability even with interference from other metal ions [56].

Fig. 5(a) describes the transfer characteristics of the TFT after Pb^{2+} addition at room temperature. The shift in V_{gs} observed after the addition of Pb^{2+} explains the coordination between aptamer and Pb^{2+}, resulting in G-quadruplex structure. Then negatively charged electrons from the aptamer backbone moves closer to the surface of the semiconductor and exhibit a negative top gating effect [57]. These electrons scatter significantly in the ZnO lattice due to high oxygen vacancies [40]. Therefore, to have a considerable current in the channel, a larger gate voltage needs to be applied to accumulate electrons to reach on-state current (I_{on}). The flat-band voltage V_{fb} now is shifted to the positive V_{gs} region indicating a highly resistive path created for the flow of electrons. When Pb^{2+} is added without the aptamer, it adsorbs on the surface of APTES through electrostatic van der Waals interaction with amine group [58, 59]. This interaction is different compared to the aptamer-Pb^{2+} which can be distinguished from the nature of the I_{ds} - V_{gs} curve. The APTES also interacts with other ions and used in Hg^{2+}, Pb^{2+} removal techniques. This signifies the use and role of aptamer to make the sensor specific to Pb^{2+}.

In a more realistic scenario, there is a need to detect Pb^{2+} from different sources of drinking water, which contains other favourable mineral ions. These ions can interfere with the sensing of Pb^{2+} and the aptaTFTs should exhibit robustness and have least affinity towards interfering agents. To mimic this condition, salts of copper (Cu^{2+}) and iron (Fe^{2+}) of 22μM and 27μM concentrations, respectively were introduced to validate the Pb^{2+} detection. Fig. 5(b) shows the I_{ds} - V_{gs} response of the aptaTFT with respect to Cu^{2+} and Fe^{2+} in comparison with Pb^{2+}. It can be clearly observed that, the I_{ds} range increases an order of magnitude while the V_{fb} shifts to the positive V_{gs} region. Even though both ions have a charge of 2+, there is a great possibility of iron present in Fe^{3+} state due to oxidation in aqueous solution. This may be a reason for the lower V_{fb} of iron.

The I-V characteristics shows the influence of aptamer after addition of Pb^{2+}. It is clearly observed that 'U' shaped curve become sharper in the form of 'V' with the influence of Pb^{2+} [Fig. 5(a & b)]. This is quite significant because of the complex formation by DNA-metal ion. The mobility of the charge carriers also alters due to the increased scattering, thereby reducing the drain current. In case of Pb^{2+}, the mobility decreases to 2×10^{-6} cm^2/Vs from 8×10^{-6} cm^2/Vs (aptamer). This kind of interpretation also helps us distinguish between the interfering ions and the desired target. As it is clearly visible from the graph, the shape of the curves for interfering ions have become much wider compared to aptamer.

The inset in Fig. 5(b) represents the V_{fb} range of the interfering ions of these ions and the error is too low, which means the device is highly specific in detecting the nature of the target. This is very important for designing portable devices which give a clear window for calibration. Fig. 5(c) describes the high selectivity for the Pb^{2+} ions in terms of change in drain current (ΔI). This is the ratio of I_{fb} of the aptamer to the I_{fb} of the target. Clearly, the change in current for Pb^{2+} is twice when compared to Fe^{2+} and Cu^{2+}. Fig. 5(d) educates about the use of the type of aptamers for sensing. The data shows the importance of using shorter sequence as the number of electron donor species (nucleobases) are reduced. The sensitivity and specificity of NHPb1 (5'-GGTTGGTGTGGTTGGTTTTTTTTTTTTTTT-NH_2-3') is less compared to NHPb (5'-GGTTGGTGTGGTTGG-NH_2-3').

Fig. 5(e) represents the effect of concentration of the aptamer on the flat-band voltage. Low concentration of aptamers favours the change in the charge distribution on the ZnO surface. However, further decrease in concentration below 1.7 nM did not alter the TFT characteristics and this trend shows the lower detection limit of the device with these aptamers. Further increase in aptamer concentration showed a decrease in the drain current, much lower than the 1.7 nM concentration. Fig. 5(f) explains the response of the TFT with respect to concentration of the Pb^{2+} target. The V_{fb} gradually decreased when exposed to higher concentrations of Pb^{2+}. Also, it is important to notice that the V_{fb} range does not overlap for the two used concentrations. The aptaTFT showed a minimal change in I-V characteristics to interfering agents, indicating that the aptamer exhibits a high selectivity to Pb^{2+} over interfering ions.

E. coli detection

G-Quadruplex forming aptamers specific for *E. coli* were identified from the following reports [60, 61].

In this work, aptamers specific to *E.coli* were modified with NH_2 at their 3' end to enable conjugation with APTES-GLU over ZnO TFTs. Of these, DH1 (5'-CCCAAGCTTGGGTATGAGAGGATAGAGGGGGG GGGAGGTGGTTAGTGTAGGGTAGGTGGGAAGT TATCGCGGATCCGCG-NH_2-3') showed better sensor response compared to GN12 (5'-ATACCAGCT TATTCAATTCCGAGTCCAGACTCACCGCCGCCT CCTCAAGACGTGCTGGAGATAGTAAGTGCAAT CT-NH_2-3'). This performance may be due to the availability of 38 guanine bases with (GC-content: 59%) in the NHDH1 sequence compared to 15 guanine bases (GC content: 59%) GN12 sequence. *Klebsiella pneumoniae* was cultured and used as an interfering agent to analyze the specificity of aptamers for detecting *E.coli*. Fig. 6(a) represents the I_{ds} – V_{gs} response of the aptaTFT to the NHEC1 (DH1), *E. coli* and *KP*. After the addition of *E. coli* enormous shifts were observed in drain current as well as in flat-band voltage as shown in Fig. 6(a).

The shift is observed after contact with bacteria, which brings the negative charges of *E. coli* close to the ZnO surface. This process dopes the surface of ZnO with electrons and the scattering increases near the surface. This lowered the concentration of electrons near the dielectric interface and was observed from the significant reduction in channel mobility from 1.2×10^{-5} to 2×10^{-6} cm^2/Vs. Therefore, one needed to apply higher positive voltage to the gate electrode to achieve on-state current in the channel. The V_{fb} shifts to the positive V_{gs} region while the current increases a little higher than an order of magnitude to μA range. The response for *E.coli* also depends on the total surface charge on the bacteria which may interfere in the conduction process. This range of current also facilitates no additional process for signal amplification for bacterial detection.

KP did not alter V_{fb} but the drain current increased due to the altering of charge distribution. Fig. 6(b) highlights the quantum of shifts in I_{ds} for *E. coli* and *KP*. It is significant to note that the order of error in shift for *E. coli* is less than 2%, which favours the sensitivity of the aptaTFT. The inset in Fig. 6(b) describes the V_{fb} shifts of the aptaTFT with different concentrations of the *E. coli*. This indicates the better sensor response at lower concentrations. Lower concentration ensures better binding and clear interaction with the aptamer.

Fig. 6(c) shows the voltage shift recorded for two aptamers. NHEC1 is an aptamer that covers the whole body of *E. coli1* and NHEC2 is specific to the outer membrane of the pathogens. AptaTFT response to the NHEC1 has a larger effect on the charge distribution than the NHEC2. This implies that the NHEC1 reaction creates a greater resistive path to the electrons, therefore we need a high V_{fb}. Fig. 6(d) shows the effect of NHEC1 concentration on V_{fb}. At the 216 nM concentration of this aptamer, the sensor response were consistent. Concentrations less than 200 nM were not ideal for sensor response and hence concentration of 216 nM were used for this experiment.

Fig. 7(a) & (b) describes the sensitivity of the TFT with respect to the aptamer and targets corresponding to Pb^{2+} and *E. coli* detection, respectively. It can be observed that the V_{fb} in the two cases are less than ±8 V. Low voltage operation prevents unwanted redox reactions in bio-molecules, and provides low power consumption. To utilize these advantages, real-time responses in this study were measured by keeping both V_{ds} and V_{gs} at 5 V. Fig. 7(c) reveals the real-time responses of the aptaTFT to various Pb^{2+} concentrations. The I_{ds} values immediately decreased after adding the higher concentration. This result suggests the introduction of various concentrations of Pb^{2+} in the aptaTFT could be detected by observing the current changes. A plausible sensing mechanism is that as the higher concentration target was added, the number of interactions with the unbounded aptamers also increased. This increasingly altered the charge distribution, resulting in a higher resistive path to the electrons. Similarly, responses were recorded for different concentrations of *E. coli* and the trend is shown in Fig. 7(d).

Fig. 8 describes the V_{fb} for other aptamers that were used. The response of NHPb1 and NHGN12 was an anomaly to the mechanism reported with the other two aptamers and needs a separate discussion. NHPb1 has a V_{fb} of and 3.95 ± 0.42 V. The NHGN12 aptamer binds to the outer membrane of the *E. coli*. It has a fairly consistent V_{fb} of 6.5 ± 0.71 V after binding with *E. coli*. It is also very crucial to acknowledge the fact that the voltages involved in sensing is between the range of ±8V DC, that is 16 V maximum. This is very helpful in designing portable devices, since many contemporary functionalized FETs work at extreme voltages. For graphene-based FETs, voltages range from ±40 V [6] to ±0.5 V [62]. However, ZnO based devices range within ∼20 V [38]. Table 1 lists the flat-band voltage for all the analytes and targets described in the bar plots.

Conclusion

This study highlights the importance of aptamer based ZnO-TFTs for detection of Pb^{2+} and *E. coli* in water. The ZnO TFT arrays are fabricated at a low-cost and acts as a robust platforms for multiplexed detection of heavy ions and pathogens in water. A range of aptamers are investigated for specificity towards the targets with the presence of interfering agents. Pb^{2+} (27 nM) and *E. coli* (10^5 cfu/ml) were detected using this platform and

it is capable of sensing a range of heavy ion concentration and pathogens by immobilizing specific aptamers in the array. V_{fb} of Pb^{2+} (2.425 ± 0.35 V), *E. coli* (6.5 ± 0.46 V) shows promising trend for reproducibility. A possibility of printing the aptamers specific to range of targets over TFTs with custom made bio-printer is underway to enhance the sensitivity and feasibility of bringing printed aptaTFTs package. This low-cost TFT array surely creates a novel path for detecting heavy metal ions and pathogens in resource limited settings.

Competing interests
The authors declare that they have no competing interests.

Author's contributions
S.K.H did formal analysis, investigation, validation, data curation and writing original draft. V.S.R acquired funding, conceptualized the work, investigated, written original draft, reviewed, and supervised. R.A investigated bacterial strains, written original draft. G.S designed fabrication methodology and validated the performance. K.R.G fine tuned fabrication methodology and provided resources. S.S and S.S.G provided resources, reviewed and edited the draft. B.O reviewed and edited the draft. D.J acquired funding, reviewed and edited the draft. All authors read and approved the final manuscript.

Acknowledgements
We acknowledge funding from Global Challenges Research Fund (GCRF), Project code: SP/GCRF-19/003 and University of Plymouth. The Bibliography

Author details
[1]Department of Instrumentation and Applied Physics, Indian Institute of Science, Bengaluru, 560012, India. [2]Wolfson Nanomaterials and Devices Laboratory, School of Engineering, Computing and Mathematics, Plymouth University, Devon, PL4 8AA, UK.

References
1. Tu, J., Gan, Y., Liang, T., Hu, Q., Wang, Q., Ren, T., Sun, Q., Wan, H., Wang, P.: Graphene fet array biosensor based on ssdna aptamer for ultrasensitive hg2+ detection in environmental pollutants. Front. Chem. **6** (2018). doi:10.3389/fchem.2018.00333
2. Zhou, G., Chang, J., Cui, S., Pu, H., Wen, Z., Chen, J.: Real-time, selective detection of pb2+ in water using a reduced graphene oxide/gold nanoparticle field-effect transistor device. ACS Appl. Mater. Interfaces. **6**(21), 19235–19241 (2014). doi:10.1021/am505275a. PMID: 25296985
3. Sayyad, P.W., Ingle, N.N., Al-Gahouari, T., Mahadik, M.M., Bodkhe, G.A., Shirsat, S.M., Shirsat, M.D.: Sensitive and selective detection of cu2+ and pb2+ ions using field effect transistor (fet) based on l-cysteine anchored pedot:pss/rgo composite. Chem. Phys. Lett. **761**, 138056 (2020). doi:10.1016/j.cplett.2020.138056
4. Luo, L., Jie, J., Zhang, W., He, Z., Wang, J., Yuan, G., Zhang, W., Wu, L.C.M., Lee, S.-T.: Silicon nanowire sensors for hg2+ and cd2+ ions. Appl. Phys. Lett. **94**(19), 193101 (2009). doi:10.1063/1.3120281
5. An, J.H., Jang, J.: A highly sensitive fet-type aptasensor using flower-like mos2 nanospheres for real-time detection of arsenic(iii). Nanoscale **9**, 7483–7492 (2017). doi:10.1039/C7NR01661A
6. Thakur, B., Zhou, G., Chang, J., Pu, H., Jin, B., Sui, X., Yuan, X., Yang, C.-H., Magruder, M., Chen, J.: Rapid detection of single e. coli bacteria using a graphene-based field-effect transistor device. Biosens. Bioelectron. **110**, 16–22 (2018). doi:10.1016/j.bios.2018.03.014
7. Salinas, R.A., Orduña-Díaz, A., Obregon-Hinostroza, O., Dominguez, M.A.: Biosensors based on zinc oxide thin-film transistors using recyclable plastic substrates as an alternative for real-time pathogen detection. Talanta **237**, 122970 (2022). doi:10.1016/j.talanta.2021.122970
8. Dey, A., Singh, A., Dutta, D., Ghosh, S.S., Iyer, P.K.: Rapid and label-free bacteria detection using a hybrid tri-layer dielectric integrated n-type organic field effect transistor. J. Mater. Chem. A **7**, 18330–18337 (2019). doi:10.1039/C9TA06359E
9. Kumar, N., Wang, W., Ortiz-Marquez, J.C., Catalano, M., Gray, M., Biglari, N., Hikari, K., Ling, X., Gao, J., van Opijnen, T., Burch, K.S.: Dielectrophoresis assisted rapid, selective and single cell detection of antibiotic resistant bacteria with g-fets. Biosens. Bioelectron. **156**, 112123 (2020). doi:10.1016/j.bios.2020.112123
10. Rehman, K., Fatima, F., Waheed, I., Akash, M.S.H.: Prevalence of exposure of heavy metals and their impact on health consequences. J. Cell. Biochem. **119**(1), 157–184 (2018). doi:10.1002/jcb.26234
11. Gorkhali, R., Huang, K., Kirberger, M., Yang, J.J.: Defining potential roles of Pb2+ in neurotoxicity from a calciomics approach. Met. Integr. Biometal Sci. **8**(6), 563–578 (2016). doi:10.1039/c6mt00038j
12. Ha, X., Yin, Q., Lue, T., Liu, B., Xu, Y., Liu, C., Yu, X.: Lead acetate in drinking water is toxic to hippocampal tissue: Measuring relative protein changes using tissue array detection. Neural Regen. Res. **5**, 519–524 (2010). doi:10.3969/j.issn.1673-5374.2010.07.007
13. Santucci, R.J., Scully, J.R.: The pervasive threat of lead (pb) in drinking water: Unmasking and pursuing scientific factors that govern lead release. Proc. Natl. Acad. Sci. **117**(38), 23211–23218 (2020). doi:10.1073/pnas.1913749117
14. Chauhan, A., Goyal, P., Varma, A., Jindal, T.: Microbiological evaluation of drinking water sold by roadside vendors of delhi, india. Appl. Water Sci. **7**, 1635–1644 (2017). doi:10.1007/s13201-015-0315-x
15. Bivins, A., Lowry, S., Murphy, H.M., Borchardt, M., Coyte, R., Labhasetwar, P., Brown, J.: Waterborne pathogen monitoring in jaipur, india reveals potential microbial risks of urban groundwater supply. npj Clean Water **3**(35) (2020). doi:10.1038/s41545-020-00081-3
16. Malche, T., Tharewal, S., Bhatt, D.P.: A portable water pollution monitoring device for smart city based on internet of things (IoT). IOP Conf. Ser. Earth Environ. Sci. **795**(1), 012014 (2021). doi:10.1088/1755-1315/795/1/012014
17. Mukherjee, S., Bhattacharyya, S., Ghosh, K., Pal, S., Halder, A., Naseri, M., Mohammadniaei, M., Sarkar, S., Ghosh, A., Sun, Y., Bhattacharyya, N.: Sensory development for heavy metal detection: A review on translation from conventional analysis to field-portable sensor. Trends Food Sci. Technol. **109**, 674–689 (2021). doi:10.1016/j.tifs.2021.01.062
18. Srivastava, S., Sharma, V.: Ultra-portable, smartphone-based spectrometer for heavy metal concentration measurement in drinking water samples. Appl. Water Sci. **11**(177) (2021). doi:10.1007/s13201-021-01519-w
19. Liao, Y.-H., Muthuramalingam, K., Tung, K.-H., Chuan, H.-H., Liang, K.-Y., Hsu, C.-P., Cheng, C.-M.: Portable device for quick detection of viable bacteria in water. Micromachines **11**(12) (2020). doi:10.3390/mi11121079
20. Singh, P., Kakkar, S., Bharti, Kumar, R., Bhalla, V.: Rapid and sensitive colorimetric detection of pathogens based on silver–urease interactions. Chem. Commun. **55**, 4765–4768 (2019). doi:10.1039/C9CC00225A
21. Shen, C., Wu, S., Meng, Q.: Construction of portable drinking water device using an agricultural biomass-derived material of polyethylenimine-grafted-corncob. Food Cont. **130**, 108375 (2021). doi:10.1016/j.foodcont.2021.108375
22. Santra, D., Mandal, S., Santra, A., Ghorai, U.K.: Cost-effective, wireless, portable device for estimation of hexavalent chromium, fluoride, and iron in drinking water. Anal. Chem. **90**(21), 12815–12823 (2018). doi:10.1021/acs.analchem.8b03337
23. Thavarajah, W., Verosloff, M.S., Jung, J.K., Alam, K.K., Miller, J.D., Jewett, M.C., Young, S.L., Lucks, J.B.: A primer on emerging field-deployable synthetic biology tools for global water quality monitoring. npj Clean Water **3**(18) (2020). doi:10.1038/s41545-020-0064-8
24. Guo, W., Zhang, C., Ma, T., Liu, X., Chen, Z., Li, S., Deng, Y.: Advances in aptamer screening and aptasensors' detection of heavy metal ions. J. Nanobiotechnology **19**(166) (2021). doi:10.1186/s12951-021-00914-4
25. McConnell, E.M., Nguyen, J., Li, Y.: Aptamer-based biosensors for environmental monitoring. Front. Chem. **8** (2020). doi:10.3389/fchem.2020.00434
26. Zeng, L., Zhou, D., Gong, J., Liu, C., Chen, J.: Highly sensitive aptasensor for trace arsenic(iii) detection using dnazyme as the biocatalytic amplifier. Anal. Chem. **91**(3), 1724–1727 (2019).

doi:10.1021/acs.analchem.8b05466
27. Wei, Y., Gao, C., Meng, F.-L., Li, H.-H., Wang, L., Liu, J.-H., Huang, X.-J.: Sno2/reduced graphene oxide nanocomposite for the simultaneous electrochemical detection of cadmium(ii), lead(ii), copper(ii), and mercury(ii): An interesting favorable mutual interference. J. Phys. Chem. C **116**(1), 1034–1041 (2012). doi:10.1021/jp209805c
28. Vu, C.-A., Chen, W.-Y.: Predicting future prospects of aptamers in field-effect transistor biosensors. Molecules **25**(3) (2020). doi:10.3390/molecules25030680
29. Raghavan, V.S., O'Driscoll, B., Bloor, J.M., Li, B., Katare, P., Sethi, J., Gorthi, S.S., Jenkins, D.: Emerging graphene-based sensors for the detection of food adulterants and toxicants – a review. Food Chem. **355**, 129547 (2021). doi:10.1016/j.foodchem.2021.129547
30. Pages, B.J., Ang, D.L., Wright, E.P., Aldrich-Wright, J.R.: Metal complex interactions with dna. Dalton Trans. **44**, 3505–3526 (2015). doi:10.1039/C4DT02700K
31. Singh, T., Shukla, S., Kumar, P., Wahla, V., Bajpai, V.K., Rather, I.A.: Application of nanotechnology in food science: Perception and overview. Front. Microbiol. **8** (2017). doi:10.3389/fmicb.2017.01501
32. Liu, Q., Zhao, C., Chen, M., Liu, Y., Zhao, Z., Wu, F., Li, Z., Weiss, P.S., Andrews, A.M., Zhou, C.: Flexible multiplexed in¡sub¿2¡/sub¿o¡sub¿3¡/sub¿ nanoribbon aptamer-field-effect transistors for biosensing. iScience **23** (2020). doi:10.1016/j.isci.2020.101469
33. Kwon, J., Lee, Y., Lee, T., Ahn, J.-H.: Aptamer-based field-effect transistor for detection of avian influenza virus in chicken serum. Anal. Chem. **92**(7), 5524–5531 (2020). doi:10.1021/acs.analchem.0c00348. PMID: 32148026
34. Nakatsuka, N., Yang, K.-A., Abendroth, J.M., Cheung, K.M., Xu, X., Yang, H., Zhao, C., Zhu, B., Rim, Y.S., Yang, Y., Weiss, P.S., Stojanović, M.N., Andrews, A.M.: Aptamer–field-effect transistors overcome debye length limitations for small-molecule sensing. Science **362**(6412), 319–324 (2018). doi:10.1126/science.aao6750
35. Aliakbarinodehi, N., Jolly, P., Bhalla, N., Miodek, A., De Micheli, G., Estrela, P., Carrara, S.: Aptamer-based field-effect biosensor for tenofovir detection. Sci. Rep. **7**(44409) (2017). doi:10.1038/srep44409
36. Hirao, T., Furuta, M., Hiramatsu, T., Matsuda, T., Li, C., Furuta, H., Hokari, H., Yoshida, M., Ishii, H., Kakegawa, M.: Bottom-gate zinc oxide thin-film transistors (zno tfts) for am-lcds. IEEE Transactions on Electron Devices **55**(11), 3136–3142 (2008). doi:10.1109/TED.2008.2003330
37. Fathil, M.F.M., Md Arshad, M.K., Ruslinda, A.R., Gopinath, S.C.B., Nuzaihan M.N., M., Adzhri, R., Hashim, U., Lam, H.Y.: Substrate-gate coupling in zno-fet biosensor for cardiac troponin i detection. Sens. Actuators B Chem. **242**, 1142–1154 (2017). doi:10.1016/j.snb.2016.09.131
38. Agarwal, D.K., Kandpal, M., Surya, S.G.: Characterization and detection of cardiac troponin-t protein by using 'aptamer' mediated biofunctionalization of zno thin-film transistor. Appl. Surf. Sci. **466**, 874–881 (2019). doi:10.1016/j.apsusc.2018.10.086
39. Salinas Domónguez, R.A., Domónguez Jiménez, M.A., Orduña Dóaz, A.: Antibody immobilization in zinc oxide thin films as an easy-handle strategy for escherichia coli detection. ACS Omega **5**(32), 20473–20480 (2020). doi:10.1021/acsomega.0c02583. PMID: 32832800
40. Saravanavel, G., Honnali, S.K., Lourdes, K.S., John, S., Gunasekhar, K.R.: Study on the thermoelectric properties of al-zno thin-film stack fabricated by physical vapour deposition process for temperature sensing. Sens. Actuators A Phys. **332**, 113097 (2021). doi:10.1016/j.sna.2021.113097
41. Majoul, N., Aouida, S., Bessaïs, B.: Progress of porous silicon aptes-functionalization by ftir investigations. Appl. Surf. Sci. **331**, 388–391 (2015). doi:10.1016/j.apsusc.2015.01.107
42. Kasprzhitskii, A., Lazorenko, G., Kruglikov, A., Kuchkina, I., Gorodov, V.: Effect of silane functionalization on properties of poly(lactic acid)/palygorskite nanocomposites. Inorganics **9**(1) (2021). doi:10.3390/inorganics9010003
43. Guang Choo, E.S., Tang, X., Sheng, Y., Shuter, B., Xue, J.: Controlled loading of superparamagnetic nanoparticles in fluorescent nanogels as effective t2-weighted mri contrast agents. J. Mater. Chem. **21**, 2310–2319 (2011). doi:10.1039/C0JM03232H
44. Matavos-Aramyan, S.: Preparation of titania/silica core-shell hybrid nanocomposites for 2024 al-alloy corrosion protection and investigation of their mechanical and thermal stability. Silicon **10**, 1601–1612 (2018). doi:10.1007/s12633-017-9644-8
45. Kocanda, M., Abdel-Motaleb, I.: Development of a dna probe using barium strontium titanate. J. Appl. Phys. **106**(12), 123916 (2009). doi:10.1063/1.3273314
46. Urmann, K., Arshavsky-Graham, S., Walter, J.G., Scheper, T., Segal, E.: Whole-cell detection of live lactobacillus acidophilus on aptamer-decorated porous silicon biosensors. Analyst **141**, 5432–5440 (2016). doi:10.1039/C6AN00810K
47. Janotti, A., de Walle, C.G.V.: Fundamentals of zinc oxide as a semiconductor. Rep. Prog. Phys. **72**(12), 126501 (2009). doi:10.1088/0034-4885/72/12/126501
48. Singh, M., Mulla, M.Y., Manoli, K., Magliulo, M., Ditaranto, N., Cioffi, N., Palazzo, G., Torsi, L., Santacroce, M.V., Franco, C.D., Scamarcio, G.: Bio-functionalization of zno water gated thin-film transistors. Proc. - 2015 8th Int. Workshop Adv. Sens. Interfaces IWASI, 261–265 (2015). doi:10.1109/IWASI.2015.7184944
49. Belagodu, T., Azhar, E.A., Yu, H.: Modulation of charge conduction in zno nanowires through selective surface molecular functionalization. Nanoscale **4**, 7330–7333 (2012). doi:10.1039/C2NR31442H
50. Kotkowiak, W., Pasternak, A.: Beyond g-quadruplexes—the effect of junction with additional structural motifs on aptamers properties. Int. J. Mol. Sci. **22**(18) (2021). doi:10.3390/ijms22189948
51. Chen, H., Sun, H., Zhang, X., Sun, X., Shi, Y., Tang, Y.: A supramolecular probe for colorimetric detection of pb2+ based on recognition of g-quadruplex. RSC Adv. **5**, 1730–1734 (2015). doi:10.1039/C4RA11395K
52. Wang, W., Kang, T.-S., Chan, P.W.H., Lu, J.-J., Chen, X.-P., Leung, C.-H., Ma, D.-L.: A label-free g-quadruplex-based mercury detection assay employing the exonuclease iii-mediated cleavage of t–hg2+–t mismatched dna. Science and Technology of Advanced Materials **16**(6), 065004 (2015). doi:10.1088/1468-6996/16/6/065004. PMID: 27877846
53. Hoang, M., Huang, P.-J.J., Liu, J.: G-quadruplex dna for fluorescent and colorimetric detection of thallium(i). ACS Sens. **1**(2), 137–143 (2016). doi:10.1021/acssensors.5b00147
54. Stoltenburg, R., Krafčiková, P., Víglaský, V., Strehlitz, B.: G-quadruplex aptamer targeting protein a and its capability to detect staphylococcus aureus demonstrated by elona. Sci. Rep. **6**(33812) (2016). doi:10.1038/srep33812
55. Wang, Z., Lu, Q., Xu, T., Wang, F., Huang, F., Peng, Y., Deng, L.: G-quadruplex-based assay combined with aptamer and gold nanoparticles for escherichia coli k88 determination. Microchim. Acta. **187**(308) (2020). doi:10.1007/s00604-020-04291-x
56. Ding, J., Zhang, D., Liu, Y., Zhan, X., Lu, Y., Zhou, P., Zhang, D.: An electrochemical aptasensor for pb2+ detection based on metal–organic-framework-derived hybrid carbon. Biosensors **11**(1) (2021). doi:10.3390/bios11010001
57. Hagen, J.A., Kim, S.N., Bayraktaroglu, B., Leedy, K., Chávez, J.L., Kelley-Loughnane, N., Naik, R.R., Stone, M.O.: Biofunctionalized zinc oxide field effect transistors for selective sensing of riboflavin with current modulation. Sensors **11**(7), 6645–6655 (2011). doi:10.3390/s110706645
58. Palos-Barba, V., Moreno-Martell, A., Hernández-Morales, V., Peza-Ledesma, C.L., Rivera-Muñoz, E.M., Nava, R., Pawelec, B.: Sba-16 cage-like porous material modified with aptes as an adsorbent for pb2+ ions removal from aqueous solution. Materials **13**(4) (2020). doi:10.3390/ma13040927
59. Nematidil, N., Sadeghi, M., Nezami, S., Sadeghi, H.: Synthesis and characterization of schiff-base based chitosan-g-glutaraldehyde/nammtnps-aptes for removal pb2+ and hg2+ ions. Carbohydr. Polym. **222**, 114971 (2019). doi:10.1016/j.carbpol.2019.114971
60. Zhang, C., Lv, X., Han, X., Man, Y., Saeed, Y., Qing, H., Deng, Y.: Whole-cell based aptamer selection for selective capture of microorganisms using microfluidic devices. Anal. Methods **7**, 6339–6345 (2015). doi:10.1039/C5AY01016K
61. Shin, H.-S., Gedi, V., Kim, J.-K., Lee, D.-k.: Detection of gram-negative bacterial outer membrane vesicles using dna aptamers. Sci. Rep. **9**(13167) (2019). doi:10.1038/s41598-019-49755-0
62. Cai, B., Wang, S., Huang, L., Ning, Y., Zhang, Z., Zhang, G.-J.:

Ultrasensitive label-free detection of pna–dna hybridization by reduced graphene oxide field-effect transistor biosensor. ACS Nano **8**(3), 2632–2638 (2014). doi:10.1021/nn4063424. PMID: 24528470

Figures

Figure 1 Thin-film transistor structure on glass substrate. **(a)** Thickness of the different layers of the TFT (top), 3D view of the TFT (bottom). **(b)** Microscopic view of the ZnO channel of length (L $\sim$ 50 μm) (top). Array of three TFTs with common gate electrode (bottom). **(c)** Fabricated device array with 78 transistors. **(d)** ZnO surface functionalized with APTES-Glutaraldehyde molecules. **(e)** Attachment of amine modified aptamers specific to lead ions to the GLU molecule. **(f)** Attachment of aptamer specific to *E. coli* and microscopic view of *E. coli* bacteria during live test.

Figure 2 Characteristics of the fabricated ZnO thin-film transistors. (a) Transfer characteristics (I_{ds} - V_{gs}) of fabricated TFT at V_{ds} = 5V. Inset shows the flat-band voltages and currents for ten devices. (b) Output characteristics (I_{ds} - V_{gs}) of the fabricated ZnO TFTs.

Tables

Table 1 Data-list of flat-band voltages of aptamers and targets used in the present work

Aptamer/Target	V_{fb} (V)
NHPb	-1.725 $\pm$ 0.11
Pb^{2+}	2.425 $\pm$ 0.35
Cu^{2+}	1.775 $\pm$ 0.035
Fe^{2+}	4.375 $\pm$ 0.03
NHEC1	-2.43 $\pm$ 0.04
E. coli	6.5 $\pm$ 0.46
KP	-2.65 $\pm$ 0.49

Additional Files

Additional File 1 — Provides detailed information about the fabrication process of thin-film transistors

Figure S1 (a) describes fabrication process flow of each layer of the TFT. (b) SEM images of the TFT channel and the magnified inset shows the morphology of the ZnO as nanoparticles. (c) XRD of ZnO describing the (002) orientation with wurtzite structure. **Figure S2** describes the secondary structures of the aptamers used in the present work. Inset shows the sequences of the aptamers along with its GC content.

Figure 3 FTIR-ATR analysis of the biofunctionalized aptaTFT. **(a)** shows the absorption peaks related to APTES binding and APTES-GLU interaction in the wavenumber range 2500 to 3500 cm^{-1}. **(b)** absorption peaks of APTES and APTES-GLU in the range 1800 to 600 cm^{-1} **(c)** and **(d)** shows NHPb aptamer interaction with glutaraldehyde. Inset shows smoothed absorption peaks of C-H alkyl spacer.

Figure 4 The AFM topographic images of the aptaTFTs. **(a & b)** shows 2D and 3D profile of APTES-GLU and APTES-GLU-DNA surface, **(c & d)** shows 2D and 3D view of APTES-GLU-DNA, **(e & f)** shows change in surface properties of ZnO TFTs after functionalization and incubation with DNA.

Figure 5 Transfer characteristics of aptaTFT as a sensor for lead detection. **(a)** shows response of aptaTFT with and without aptamer. (Inset describes the flat-band voltages in this case). **(b)** shows the characteristics of aptaTFT in presence of interfering agents such as copper and iron. Inset describes the flat-band voltages in this case). **(c)** shows the specificity with Pb^{2+} ions. **(d)** describes the specificity and sensitivity to a particular aptamer for lead. **(e)** shows the response to different concentrations of aptamer NHPb. **(f)** describes the sensitivity to different concentrations of lead.

Figure 6 Transfer characteristics of aptaTFT as a sensor for *E. coli* detection. **(a)** shows response of aptaTFT for *E. coli* and *KP*. **(b)** shows the specificity of aptaTFT to *E. coli* in presence of interfering agent. Inset describes the sensitivity to different concentrations of *E. coli*. **(c)** shows the response to different aptamers. **(d)** describes the response to different concentrations of NHEC1 aptamer.

Figure 7 **(a)** shows the flat-band voltages for various aptamers and targets used fort lead and **(b)** for *E. coli* detection. **(c)** shows the time dependent detection method for different concentrations of lead and **(d)** for *E. coli*.

Figure 8 Flat-band voltages for the aptamers NHPb1 and NHGN12.

Figures

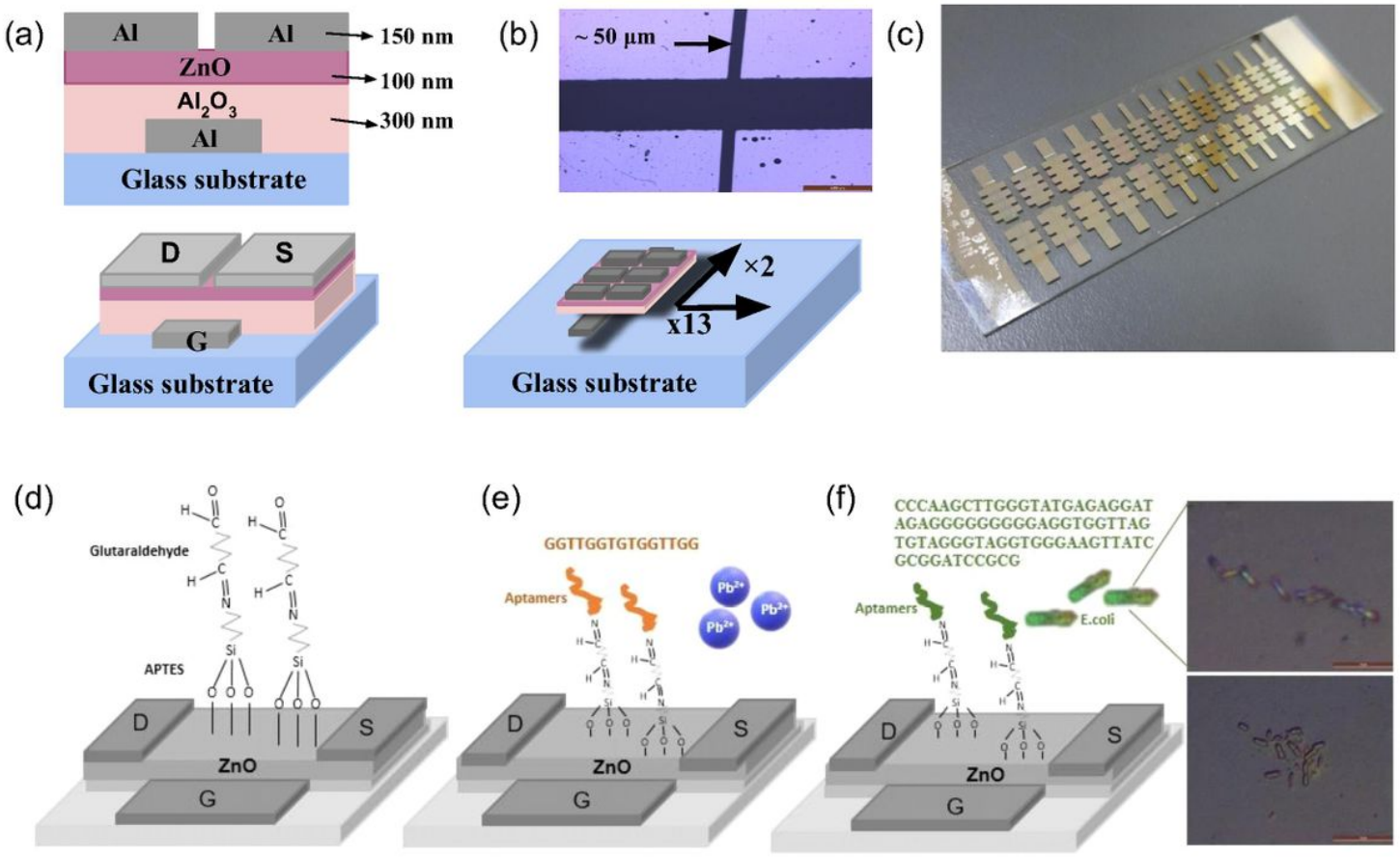

Figure 1

Thin-film transistor structure on glass substrate. (a) Thickness of the different layers of the TFT (top), 3D view of the TFT (bottom). (b) Microscopic view of the ZnO channel of length (L ≈ 50 µm) (top). Array of three TFTs with common gate electrode (bottom). (c) Fabricated device array with 78 transistors. (d) ZnO surface functionalized with APTES-Glutaraldehyde molecules. (e) Attachment of amine modified aptamers specific to lead ions to the GLU molecule. (f) Attachment of aptamer specific to E. coli and microscopic view of E. coli bacteria during live test.

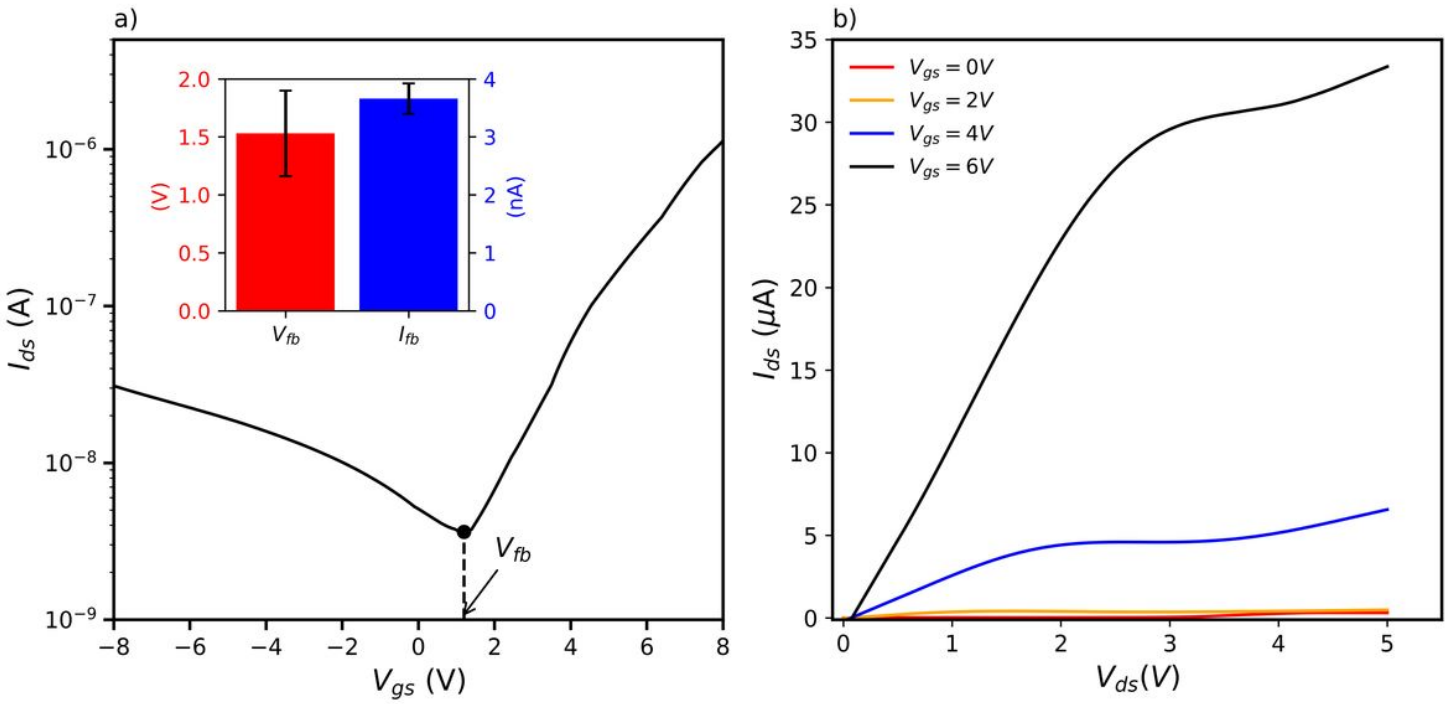

Figure 2

Characteristics of the fabricated ZnO thin-film transistors. (a) Transfer characteristics (Ids - Vgs) of fabricated TFT at Vds = 5V. Inset shows the flat-band voltages and currents for ten devices. (b) Output characteristics (Ids - Vgs) of the fabricated ZnO TFTs.

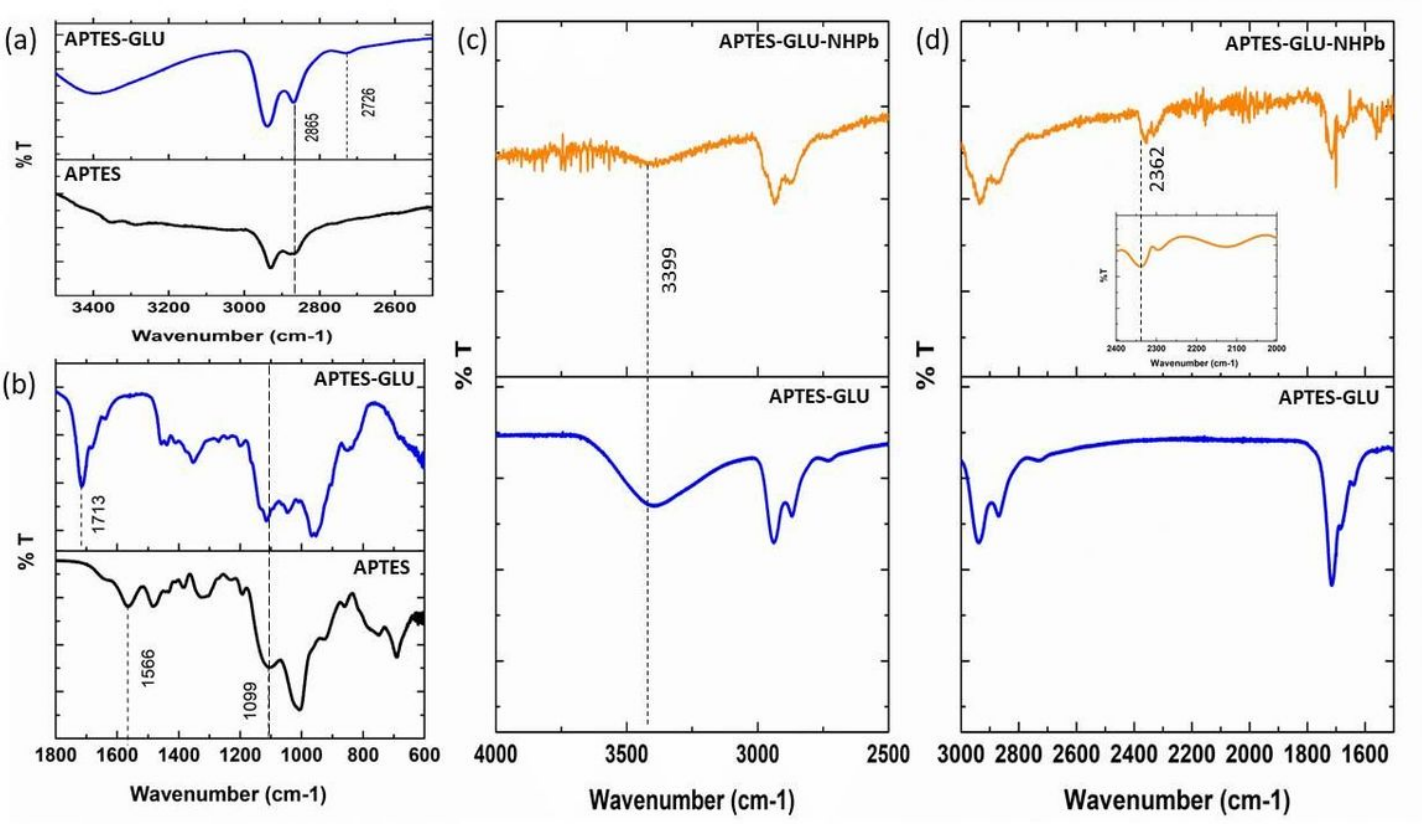

Figure 3

FTIR-ATR analysis of the biofunctionalized aptaTFT. (a) shows the absorption peaks related to APTES binding and APTES-GLU interaction in the wavenumber range 2500 to 3500 cm-1. (b) absorption peaks of APTES and APTES-GLU in the range 1800 to 600 cm-1 (c) and (d) shows NHPb aptamer interaction with glutaraldehyde. Inset shows smoothed absorption peaks of C-H alkyl spacer.

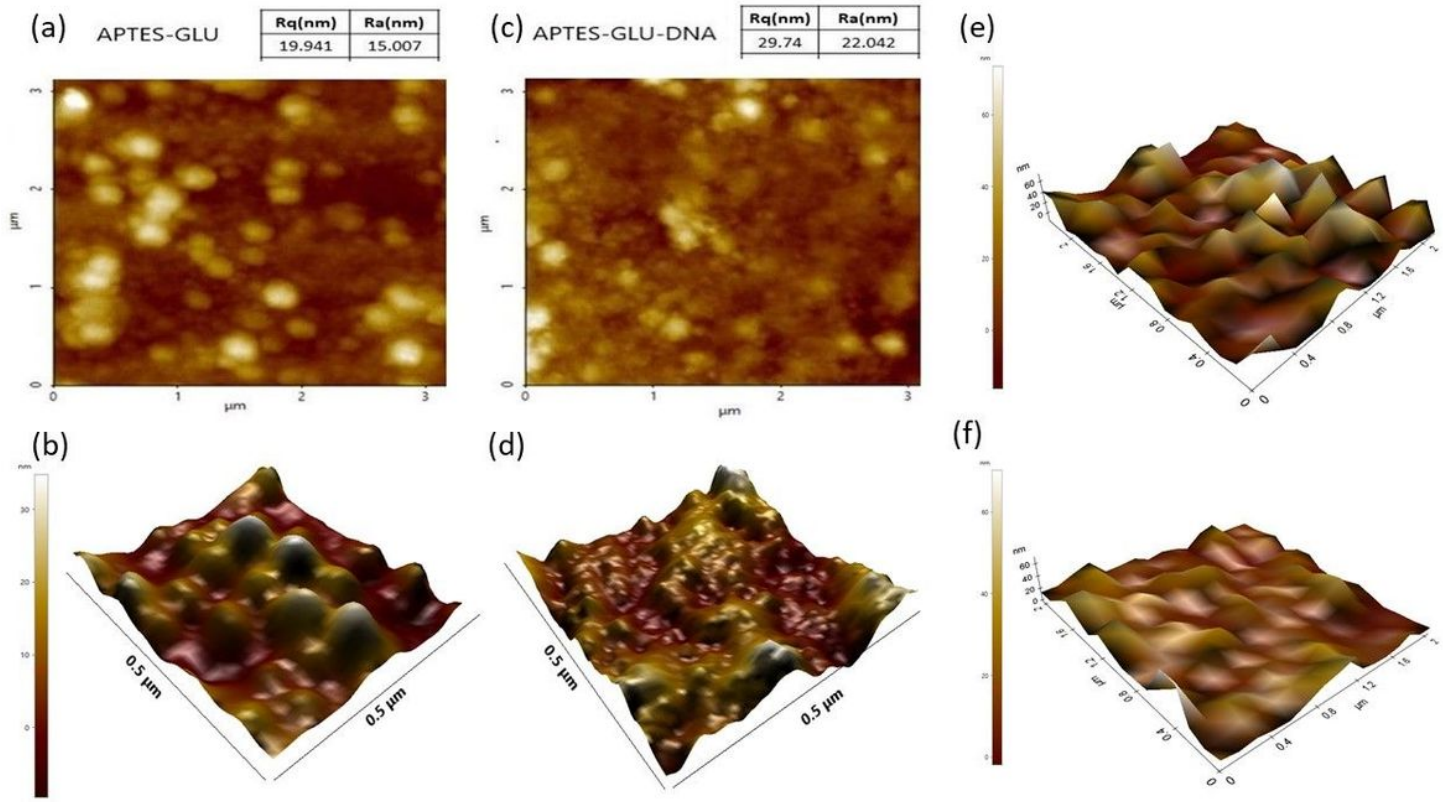

Figure 4

The AFM topographic images of the aptaTFTs. (a & b) shows 2D and 3D profile of APTES-GLU and APTES-GLU-DNA surface, (c & d) shows 2D and 3D view of APTES-GLU-DNA, (e & f) shows change in surface properties of ZnO TFTs after functionalization and incubation with DNA.

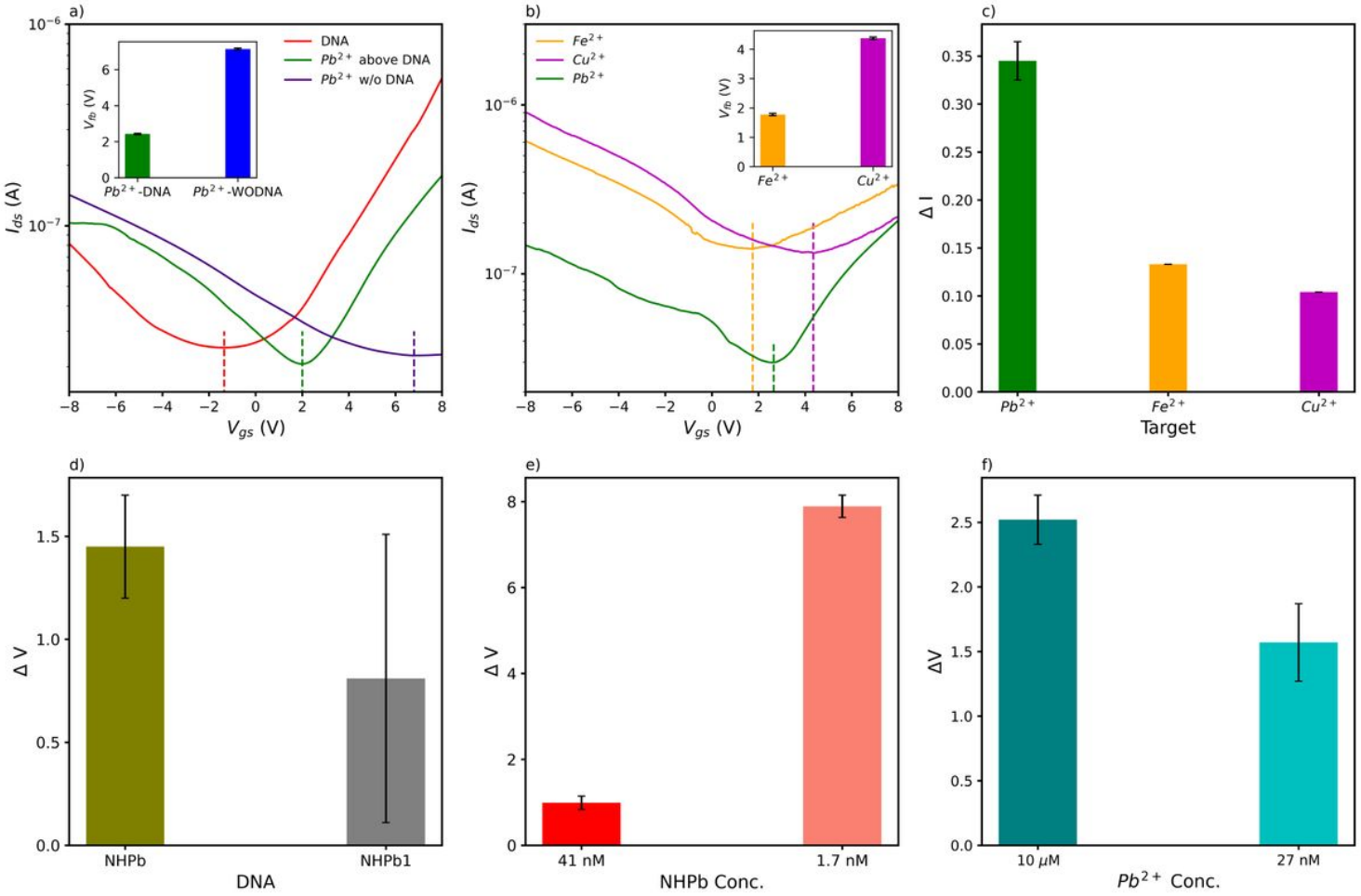

Figure 5

Transfer characteristics of aptaTFT as a sensor for lead detection. (a) shows response of aptaTFT with and without aptamer. (Inset describes the flat-band voltages in this case). (b) shows the characteristics of aptaTFT in presence of interfering agents such as copper and iron. Inset describes the flat-band voltages in this case). (c) shows the specificity with Pb2+ ions. (d) describes the specificity and sensitivity to a particular aptamer for lead. (e) shows the response to different concentrations of aptamer NHPb. (f) describes the sensitivity to different concentrations of lead.

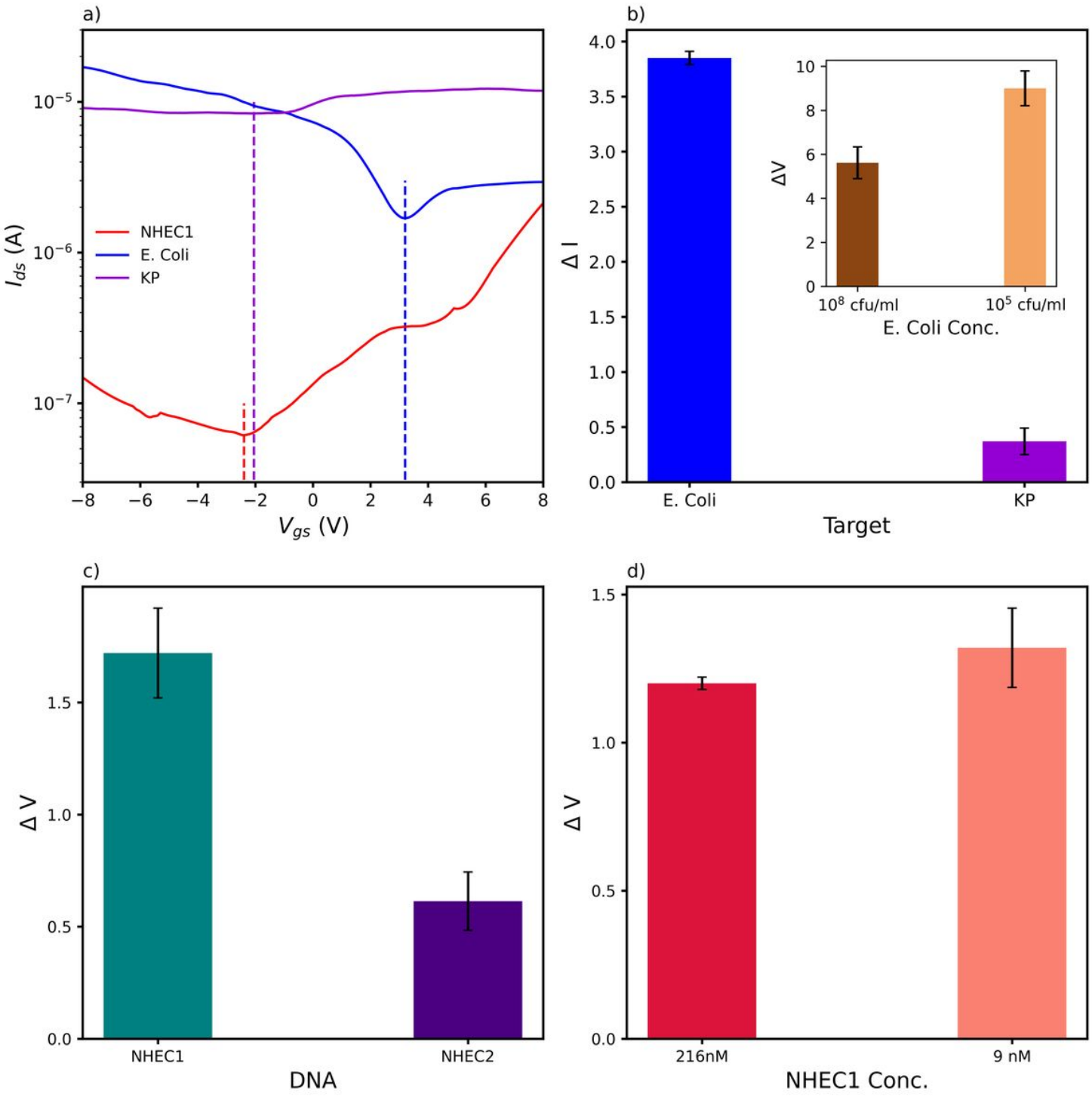

Figure 6

Transfer characteristics of aptaTFT as a sensor for E. coli detection. (a) shows response of aptaTFT for E. coli and KP. (b) shows the specificity of aptaTFT to E. coli in presence of interfering agent. Inset describes the sensitivity to different concentrations of E. coli. (c) shows the response to different aptamers. (d) describes the response to different concentrations of NHEC1 aptamer.

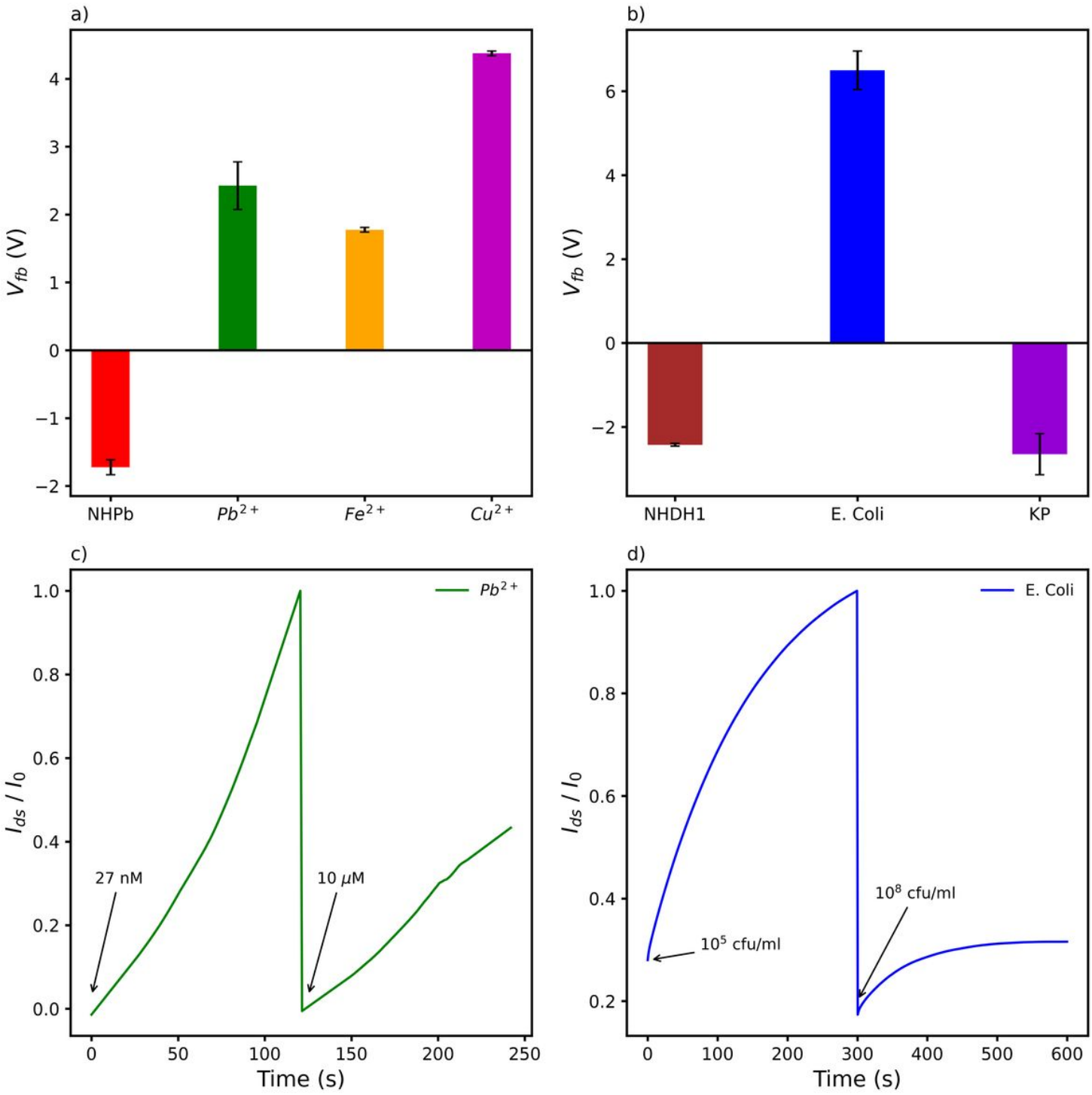

Figure 7

(a) shows the flat-band voltages for various aptamers and targets used fort lead and (b) for E. coli detection. (c) shows the time dependent detection method for different concentrations of lead and (d) for E. coli.

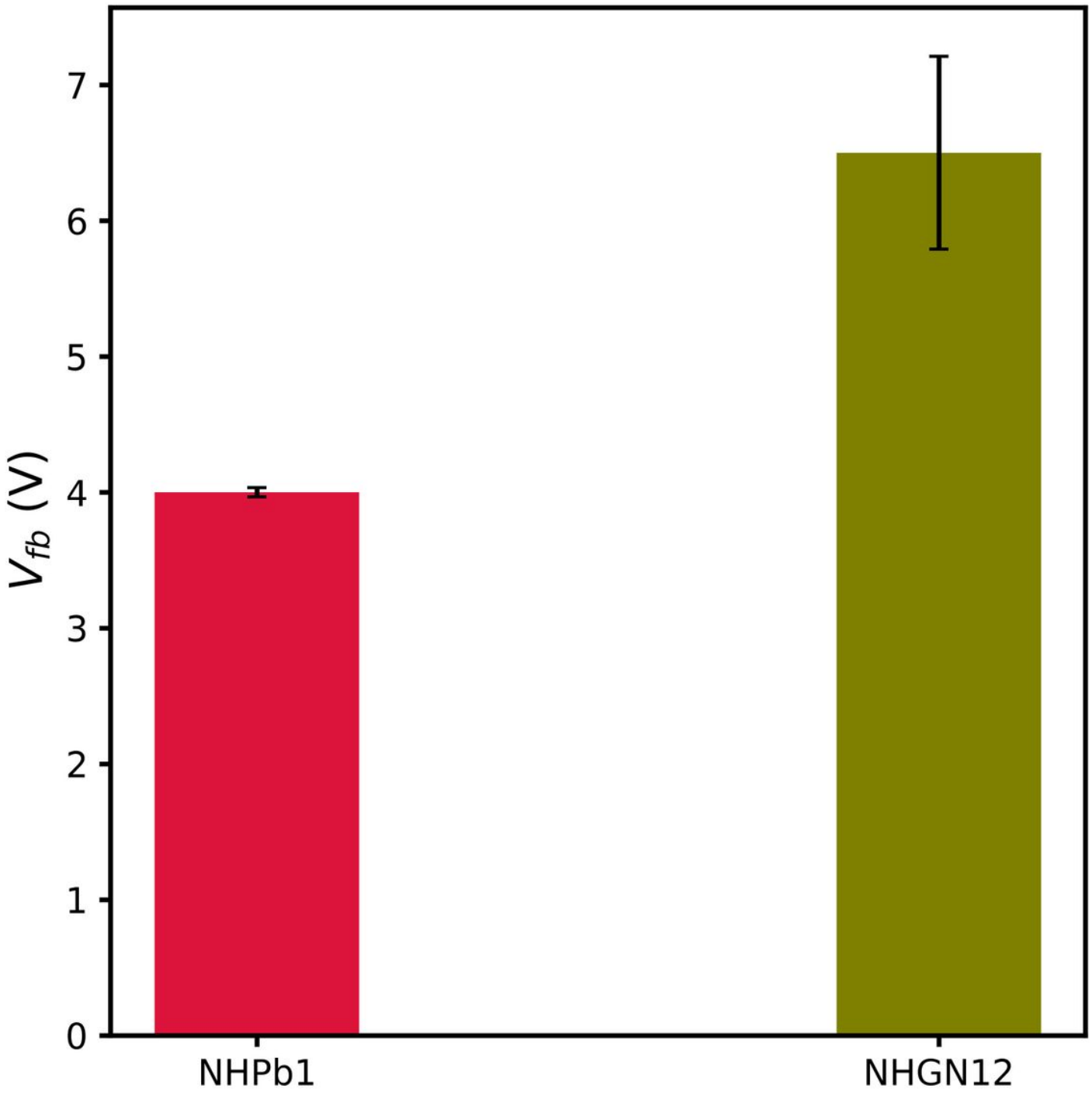

Figure 8

Flat-band voltages for the aptamers NHPb1 and NHGN12.

Supplementary Files

This is a list of supplementary files associated with this preprint. Click to download.

- AdditionalFile1.pdf
- FigS1.jpg
- FigS2.jpg